

Processing Strategies for Time-Course Data Sets in Functional MRI of the Human Brain

Peter A. Bandettini, A. Jesmanowicz, Eric C. Wong, James S. Hyde

Image processing strategies for functional magnetic resonance imaging (fMRI) data sets acquired using a gradient-recalled echo-planar imaging sequence are considered. The analysis is carried out using the mathematics of vector spaces. Data sets consisting of N sequential images of the same slice of brain tissue are analyzed in the time-domain and also, after Fourier transformation, in the frequency domain. A technique for thresholding is introduced that uses the shape of the response in a pixel compared with the shape of a reference waveform as the decision criterion. A method is presented to eliminate drifts in data that arise from subject movement. The methods are applied to experimental fMRI data from the motor-cortex and compared with more conventional image-subtraction methods. Several finger motion paradigms are considered in the context of the various image processing strategies. The most effective method for image processing involves thresholding by shape as characterized by the correlation coefficient of the data with respect to a reference waveform followed by formation of a cross-correlation image. Emphasis is placed not only on image formation, but also on the use of signal processing techniques to characterize the temporal response of the brain to the paradigm.

Key words: functional MRI; echo planar imaging; image processing; motor cortex.

INTRODUCTION

The local increase in average cerebral blood oxygenation (1, 2) that occurs upon neuronal firing is noninvasively detectable by functional magnetic resonance imaging (fMRI). Brain tissue T_2^* (3–8) and T_2 (7–10) have been found to be sensitive to cerebral blood oxygenation changes. The activation-induced increase in brain oxygenation decreases intravascular deoxyhemoglobin, and, therefore, decreases susceptibility-induced intravoxel dephasing. Spin coherence increases, resulting in increased signal intensity. Brain activation is observed as localized signal enhancement in images obtained using sequences that are sensitive to the small increases in T_2^* and T_2 that occur locally with increase in blood oxygenation.

Localized MR signal enhancement in specific brain regions that corresponds with specific neuronal tasks has

been observed by several groups using several types of sequences, including gradient-echo echo-planar imaging (EPI) at 1 T (11), 1.5 T (12, 13), 2.1 T (14), and 4 T (15); spin-echo EPI at 1.5 T (8, 9); and conventional gradient-echo imaging at 1.5 T (16–19), 2 T (20, 21), and 4 T (22, 23).

The activation-induced signal change has a magnitude and time delay determined by an imperfectly understood transfer function of the brain. This transfer function may be characterized by variables independent of brain activity and variables dependent on brain activity. Activity-independent variables that are likely to be relevant include the baseline values of blood pressure, hematocrit, blood volume, blood pO_2 , perfusion rate, vascular tone, and neuronal metabolic rate. Activity-dependent variables include vasodilation magnitude, location, and activated changes in the values of blood volume, blood oxygenation, blood perfusion, and neuronal metabolic rate, all of which may be affected by the number and firing rate of individual neurons. On the basis of the current literature, the most robust and repeatable signal enhancement is found in the primary motor and visual cortices, M1 and V1. The percent signal change in activated primary brain regions at optimal TE for maximum functional contrast ($TE \approx T_2^*$ or T_2 of gray matter) (8, 9, 14) is in the range of 1–5% at 1.5 T (12, 13), 1.5–5% at 2 T (20, 21), and 5–20% at 4 T (15, 22, 23). The delay in the signal change is 5 to 8 s from stimulus onset to 90% maximum, and 5 to 9 s from stimulus cessation to 10% above baseline (12, 14, 19, 20, 24, 25). The rise of the signal has been approximately characterized as an exponential function of time (12).

Images depicting activation induced brain function are generally created by subtraction of magnitude images obtained during a resting state from magnitude images of the same tissue obtained during activation (12, 19–23). As the number of images used for averaging increases, the time of imaging increases, allowing other physiological processes (i.e., gross motion, pulsatile blood and CSF flow, and pulsatile brain motion) to contribute to artifactual signal changes unrelated to induced neuronal activity. These artifactual signal changes, if not removed, contaminate the images. Simple image subtraction neglects useful information contained in the time response of the activation-induced signal change, and is, therefore, an ineffective means to differentiate artifactual from activation-induced signal enhancement. Use of a time course of single-shot echo-planar images in combination with control of the brain-activation timing results in data that can be processed in ways that permit differentiation of activation from artifact. Several methods to obtain high contrast-to-noise brain function images that are artifact-free are described here.

MRM 30:161–173 (1993)

From the Biophysics Research Institute, Medical College of Wisconsin, Milwaukee, Wisconsin.

Address correspondence to: James S. Hyde, Ph.D., Biophysics Research Institute, Medical College of Wisconsin, 8701 Watertown Plank Road, Milwaukee, WI 53226.

Received February 1, 1993; revised April 15, 1993; accepted April 15, 1993.

This work was supported by Grant CA41464 from the National Institutes of Health. PAB thanks GE Medical Systems, Waukesha, for financial support.

0740-3194/93 \$3.00

Copyright © 1993 by Williams & Wilkins

All rights of reproduction in any form reserved.

The brain-function image formation strategies introduced in this paper make use of a time-course of sequentially obtained single-shot echo-planar images of the same plane. The data set is a block of two spatial dimensions and one temporal dimension. A thresholding technique that uses the *shape* of the time-course signal for the decision criterion is introduced and described. Data are examined both in the time domain and, through Fourier transformation of the time-course data in each pixel of the data set, in the frequency domain. A motor cortex activation paradigm is used to compare the postprocessing strategies of simple image subtraction, temporal cross-correlation, and Fourier analysis, and to illustrate the effectiveness of the thresholding technique. The number of cycles of the finger tapping activation paradigm was also varied to illustrate characteristics of the Fourier analysis. Lastly, fMRI display methods are discussed.

EQUIPMENT AND PULSE SEQUENCE

Imaging was performed on a standard clinical GE 1.5 T Signa scanner using a 30.0-cm i.d. three-axis balanced-torque head gradient coil designed for rapid gradient switching (26), and a shielded elliptical endcapped quadrature transmit/receive birdcage RF coil designed for high-sensitivity whole-volume brain imaging (27). A single-shot blipped gradient-echo EPI sequence having an initial $\pi/2$ pulse and an effective TE ($(k_x, k_y) = (0, 0)$) of 40 ms was used. The data acquisition period was 40 ms. Dephasing lobes were placed immediately prior to the data acquisition period to minimize the flow and motion sensitivity within each image. The FOV was 24 cm, slice thickness 10 mm, and matrix 64×64 ; giving voxel dimensions of $3.75 \text{ mm} \times 3.75 \text{ mm} \times 10 \text{ mm}$. For display, images were interpolated to 256×256 . Typically, 128 images of the same plane were collected sequentially with an intra-scan temporal spacing or TR of 2 s.

THEORY

We consider a data set consisting of N images acquired from the same slice of tissue at equally spaced intervals of time. We explicitly do not consider combining and processing of multiple data sets from a particular individual or from a number of individuals. The mathematical development is carried out using the vocabulary of vector spaces (28).

Functional response to a typical motor cortex activation paradigm serves to illustrate the nature of the data more specifically. Figure 1 displays the first image in the time course. Regions A and B cover the right and left motor cortices, respectively. The time course consisted of 128 images and lasted 4 min 16 s. The activation paradigm was self-paced sequential tapping of fingers to the thumb. Starting with image #5, the subject was instructed to tap the right fingers for eight images (16 s),

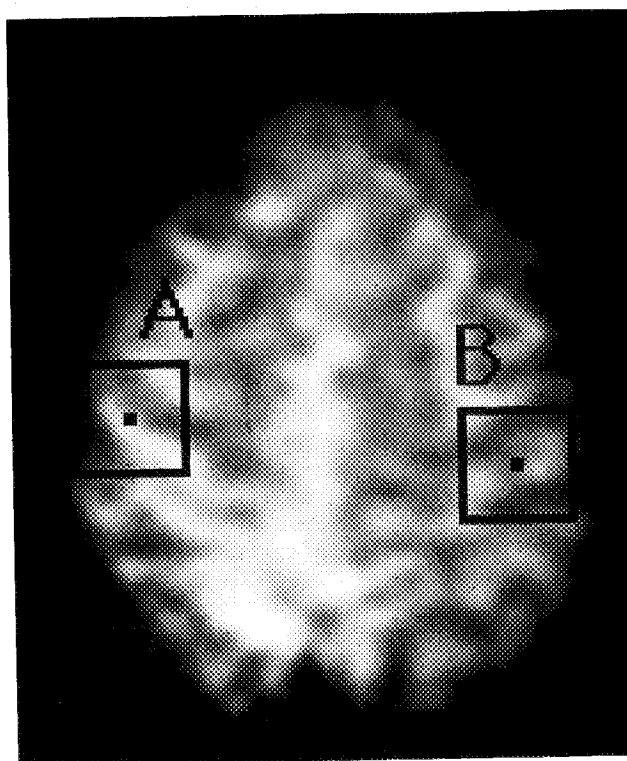


FIG. 1. Axial image containing the motor cortices. Voxel dimensions are $3.75 \times 3.75 \times 10 \text{ mm}$, $TR/TE = \infty/40$. This is the first image from the echo-planar time-course series and is used as an anatomical reference. The high signal intensity from CSF highlights contours of the sulci. Boxes A and B are 7×7 pixel regions presumably covering the right and left motor cortices, respectively. The spectral-spatial and temporal-spatial plots, shown in Figs. 2 and 3, are from the boxed regions. The time-course and spectral plots shown in Figs. 5, 8, and 10 are from the center pixel in each box.

then immediately to tap the left fingers for eight images and so on, until the end of the time course. Figures 2a and 2b are 7×7 pixel time-course displays corresponding to the boxed regions of Fig. 1. The combination of spatial and temporal information in Figs. 1 and 2 allows easy identification of temporally correlated signals in active brain regions.

In the display of Fig. 2, the lowest value of the N data points in each pixel has been set to zero. Thus, the signal intensity offsets of the data in the various pixels of Fig. 2 with respect to true zero are, in general, different. Data corresponding to the first several images in the time course are acquired before magnetization has reached equilibrium. These points are present in the display of Fig. 2, but are usually deleted manually during image processing. We call Fig. 2a "temporal-spatial" display since the data are in the time domain. All data are positive and displayed to the same scale.

It may be desirable to create an alternative display for visual inspection by forming the magnitude of the Fourier transform of the data in each pixel of Fig. 2. The cyclic and interleaved time response induced by the interleaved hand modulation of the finger-tapping task is appropriate for Fourier analysis (29).

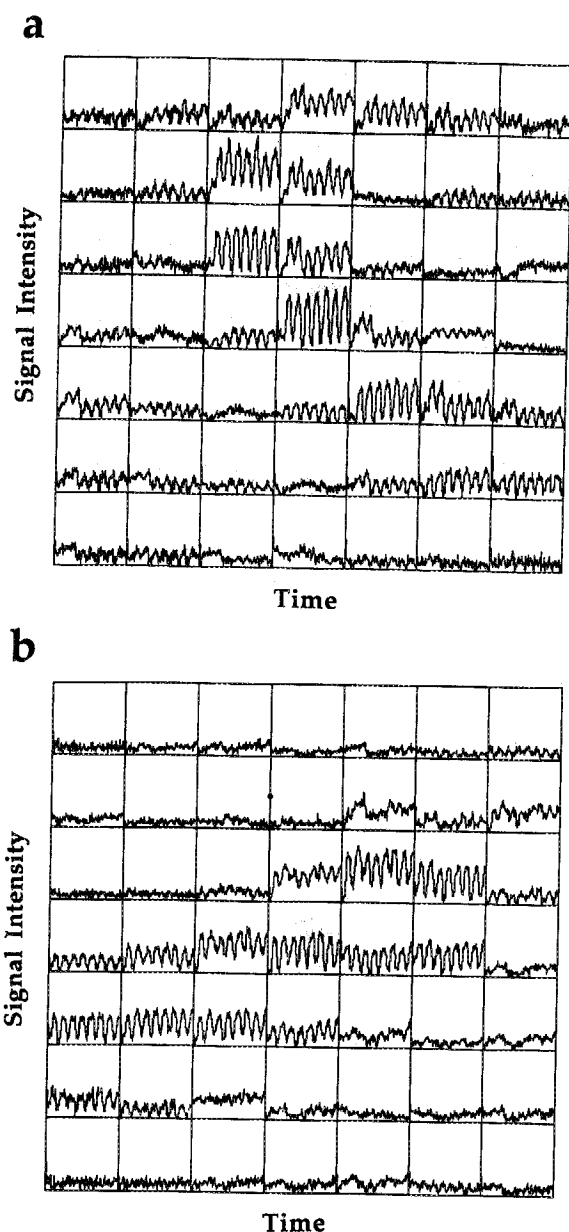


FIG. 2. Temporal-spatial plots from the 7×7 pixel boxes in Fig. 1. The active regions, revealed by the signal changes temporally correlated to the activation time course, are sharply outlined. (a) Plot from Box A, covering the right motor cortex. (b) Plot from Box B, covering the left motor cortex.

In order to produce such a display, the first few data points in a given pixel are deleted as determined by inspection of the data: five such points is typical. The vertical axis is then redefined such that zero corresponds to the average value of the remaining data. The data are then shifted to the left and zeros added as required to arrive at a number of points that is equal to a power of two, usually 128. This procedure avoids truncation artifacts. The FT is calculated assuming that the signal is real.

Figures 3a and 3b show the magnitude of the Fourier transform of the time response in Figs. 2a and 2b. In the process of forming the magnitude, phase information is

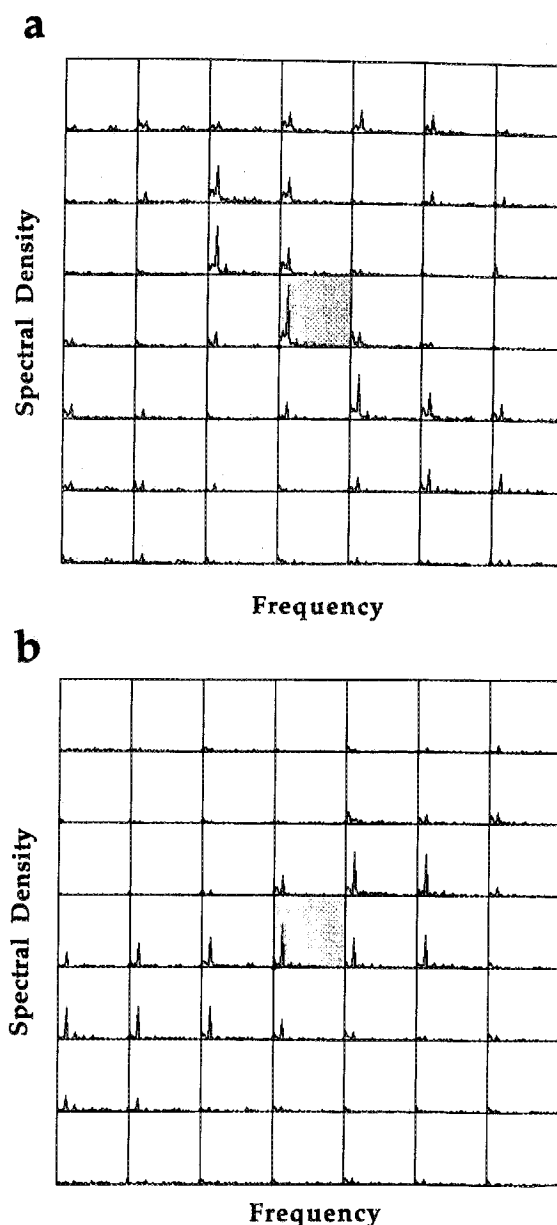


FIG. 3. Spectral-spatial plots from the 7×7 pixel boxes in Fig. 1. Application of the Fourier transform to each pixel in the time-course data set gives a sharp peak at the activation frequency. (a) Plot from Box A, covering the right motor cortex. (b) Plot from Box B, covering the left motor cortex.

lost, and, therefore, Fig. 3 intrinsically contains less information than Fig. 2. We refer to the display of Fig. 3 as "spectral-spatial," since the data in Fig. 3 are in the frequency domain.

Signal processing begins with the data in either a temporal-spatial or spectral-spatial display. There are two objectives of signal processing in functional magnetic resonance imaging: mapping of the response onto an anatomical image, and characterizing the temporal response. The time-domain data of Fig. 2 as well as the frequency-domain data of Fig. 3 can be of value in achieving each of these objectives.

Key to our approach is formation of the correlation

coefficient, cc , for each pixel.

$$cc = \frac{\sum_{i=1}^N (f_i - \mu_f)(r_i - \mu_r)}{\left[\sum_{i=1}^N (f_i - \mu_f)^2 \right]^{1/2} \left[\sum_{i=1}^N (r_i - \mu_r)^2 \right]^{1/2}} \quad [1]$$

Here f_i ($i = 1 \dots N$) is the time-course function in a given pixel. It can be considered to be an N dimensional vector. There is no requirement that N be a power of 2 for temporal data in calculating the correlation coefficient. A reference waveform or vector is denoted by r_i . This reference may be an experimental time-course function \mathbf{f} in some particular pixel or an average of several experimental \mathbf{f} s, which is then correlated with the \mathbf{f} s in other pixels. Alternatively, it could be synthesized (13). Terms μ_f and μ_r are the average values of Vectors \mathbf{f} and \mathbf{r} , respectively.

It is instructive to carry through an analysis of Eq. [1] in vector-space vocabulary. Define in N dimensional vector space a diagonal Vector \mathbf{d} of unit length (i.e., all coefficients equal to $N^{-1/2}$). See Fig. 4a. Then the average value μ_f of the function \mathbf{f} can be written:

$$\mu_f = \frac{1}{N} \sum_{i=1}^N f_i = \frac{1}{N^{1/2}} \mathbf{d} \cdot \mathbf{f}. \quad [2]$$

We define a vector μ_f , which has values of μ_f along every axis and is therefore along \mathbf{d} and of magnitude $N^{1/2} \mu_f$. Vector μ_f represents the average value of \mathbf{f} . A similar definition is made for vector μ_r . We define new vectors

$$\sigma_f = \mathbf{f} - \mu_f \quad \text{and} \quad \sigma_r = \mathbf{r} - \mu_r. \quad [3]$$

In classical statistics, the standard deviation of function f , $(SD)_f$, is given by

$$(SD)_f = \left[\frac{1}{N-1} \sum_{i=1}^N (f_i - \mu_f)^2 \right]^{1/2} \quad [4]$$

and similarly for reference function r . It is noted that the magnitudes of vectors σ_f and σ_r , denoted σ_f , σ_r , are pro-

portional to the corresponding standard deviations. See Eq. [5].

$$(SD)_{f,r} = \frac{N-1}{N^{1/2}} \sigma_{f,r} \quad [5]$$

Vectors σ_f and σ_r are orthogonal to \mathbf{d} , see Fig. 4a, which means only that the averages of the values of their components are zero. This is the simplest and nearly trivial example of orthogonalization of vectors according to the Gram-Schmidt process (28), and is equivalent to shifting the zero of the original data in a pixel such that the average is zero. vector σ_f contains the functional magnetic resonance information and vector σ_r is the corresponding reference vector. In vector-space notation, Eq. [1] can be written:

$$cc = \frac{\sigma_f \cdot \sigma_r}{\sigma_f \sigma_r}. \quad [6]$$

For the purpose of producing functional magnetic resonance images, a "thresholding" technique has been developed. Thresholding suppresses not only noise, but also eliminates spurious correlation in pixels with very large signal changes arising from pulsatile blood and cerebral spinal fluid (CSF) flow (30). A map of zeros and ones of dimensionality the same as the image's is produced. "Ones" are assigned to pixels that have time-course shapes that are similar to that of σ_r and "zeros" to the other pixels. The data set is multiplied by the map. Data that survive are subject to further processing.

The value of cc always varies between +1 and -1. A threshold value TH between 0 and +1 is selected; and data in each pixel where

$$|cc| < TH \quad [7]$$

are rejected (i.e., set to zero). The correlation coefficient is a measure of the correspondence of the shapes of the reference waveform and the functional waveform.

This thresholding process can be viewed more intuitively using the vocabulary of vector space. The angle α between the vectors σ_f and σ_r is

$$\alpha = \cos^{-1} \left| \frac{\sigma_f \cdot \sigma_r}{\sigma_f \sigma_r} \right|. \quad [8]$$

A threshold value TH implies acceptance of data when

$$\alpha < \cos^{-1}(TH). \quad [9]$$

A value for TH of 0.7 (Eq. [7]) corresponding to an angle α of 45° is a typical and useful threshold. The smaller the angle α , the more closely the shapes resemble each other. Thresholding, as described here, can be carried out using either the time-domain data or the frequency-domain data. We have tended, in our laboratory, to prefer thresholding using time-domain data as in Fig. 2, since it involves fewer computational steps and phase information is preserved in the data.

A common artifact in functional magnetic resonance imaging is a linear drift of the signal with respect to time, which seems to arise from slight patient motion during

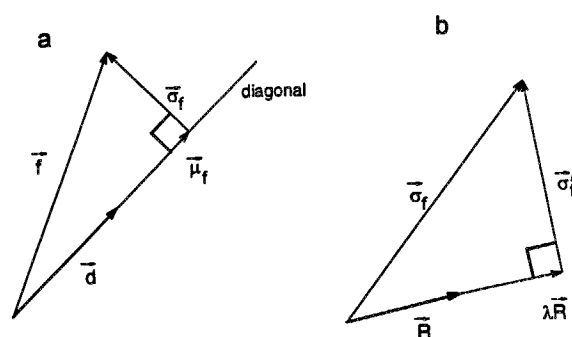


FIG. 4. Vector space diagrams. (a) Projection of the time-course data \mathbf{f} onto the diagonal vector \mathbf{d} provides a definition of vectors μ_f and σ_f . The average value of \mathbf{f} is given by $|\mu_f| N^{-1/2}$. The standard deviation vector σ_f contains functional information. (b) Orthogonalization of σ_f with respect to drift vector \mathbf{R} in order to arrive at σ'_f , a vector that no longer contains the drift artifact.

the approximately 2 min over which the data set is acquired and also to be associated with large gradients of image intensity. It is more frequently observed in neurologic patients and less frequently in well-motivated volunteers. In these cases, functional waveforms in the temporal-spatial display are readily recognized by eye, superimposed on a linear ramp. However, correlations with respect to the reference waveform can be very greatly reduced. This type of artifact is readily eliminated from the data by orthogonalization of vectors according to the Gram-Schmidt process (28). The drift is described by a vector, and the component of σ_f that is orthogonal to the drift vector is determined.

The linear drift in the data σ_f is described as the artifactual addition to the true data σ'_f of a signal that varies linearly in index i (i.e., time) and has average value 0. We can write, in vector notation,

$$\sigma_f = \sigma'_f + \lambda R. \quad [10]$$

Vector R describes the linear drift or Ramp, and is normalized. See Fig. 4b where the relevant geometry is illustrated. The Gram-Schmidt process is designed to find vector σ'_f , which will be orthogonal to R and, therefore, no longer contain the drift.

Vector R is known and the problem is to find λ . In addition to Eq. [10], we can write

$$R \cdot (\sigma_f - \lambda R) = 0 \quad [11]$$

or

$$\sigma'_f = \sigma_f - (R \cdot \sigma_f)R. \quad [12]$$

Equations [4–11] describe the elimination of constants and ramps from the original data using Gram-Schmidt orthogonalization. The orthogonalization procedure can readily be generalized to eliminate any function from the original data. It is remarked that drift might also be related to brain activity in some situations. It would be possible to produce an image from the values of λ .

FMR images can be produced in a variety of ways. The most powerful for high quality images is the use of Eq. [6] to form cc on the data of each pixel that has passed the thresholding mask. The correlation coefficient suppresses relative amplitude information. The value cc characterizes the shape; identical shapes, but different amplitudes would have the same correlation coefficients. One can produce an image from cc , but if relative amplitude information is displayed, the data in each pixel must be multiplied by σ_f/σ_r . We call such an image a "cross-correlation image." This is a preferred display. In this laboratory, we sometimes refer to the correlation coefficient images as "normalized" and to the cross-correlation image as "un-normalized." If linear drifts have been removed, σ'_f and σ'_r should be used rather than σ_f and σ_r both for thresholding and for formation of the cross-correlation image. The reference function can also be shifted systematically in small increments of time, which may prove useful in comparing the temporal responses of various brain regions.

As an alternative approach, cross-correlation images following Eq. [1] can be formed using the frequency-domain data. Thresholding as described here can be combined with the conventional image display techniques of subtraction of any two images in the original data set, or averaging any two groups of images in the original data set and subtracting them.

If the heart rate is constant during the time of acquisition, artifactual periodic signals can occur that appear in the frequency domain display as a spurious peak unrelated to the stimulation paradigm but dependent on the choice of TR . One can, in fact, produce an image using the amplitude of the signal at this frequency in each pixel in the spectral display, which highlights major arteries

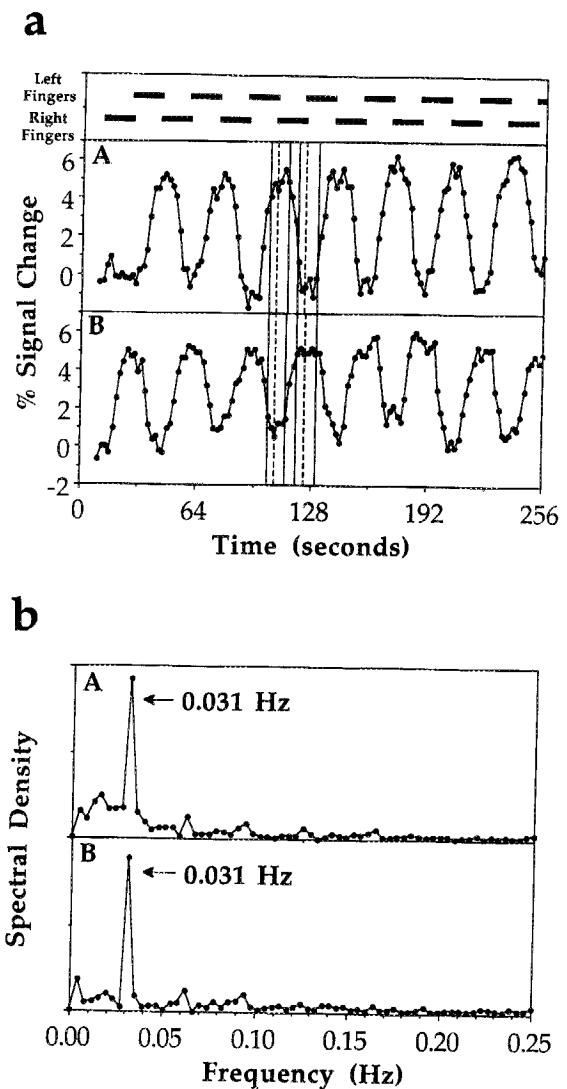


FIG. 5. Plots from the center pixels in Fig. 1. The activation paradigm of interleaved alternating hand finger movement is shown at the top. The on/off cycle rate is 0.031 Hz. (a) Plots from the center pixels in Boxes A and B show close correspondence to the left and right finger movements, respectively. (b) Plots of the spectral density versus frequency from the center pixels in Boxes A and B reveal sharp peaks at the same frequency, 0.031 Hz. The maximum oscillation frequency detectable, 0.25 Hz, is the Nyquist frequency (NF), and is determined by $NF = 1/(2 \times TR)$.

and regions of CSF. The peak that appears close to zero frequency in some pixels of Fig. 3 may be such an artifact. Gram-Schmidt orthogonalization could be used to eliminate periodic signals that are present in the data in situations where the reference function is formed from data in a pixel or group of pixels. However, if the periodic signal is absent in the reference function, it will be automatically suppressed in the correlation image.

RESULTS

Activation Paradigm

We consider the response to the activation paradigm used to obtain Fig. 2 in more detail. Figure 5 displays the time course of the center pixels in boxed regions A and B of Fig. 1 along with the timing of the activation paradigm and the corresponding Fourier transforms. Although a delay is present between stimulus and activation, the relative phase of the signal enhancement between hands and the magnitude of the signal enhancement remains relatively constant. The boxed regions A and B cover, presumably, the right and left motor cortices, respectively. The signal enhancement from each box follows the activation timing from the contralateral hand.

Subtraction

Images 54 and 62, illustrated by the dotted lines in Fig. 5a, were obtained during periods of peak signal enhancement for the right and left motor cortices, respectively. The image obtained by subtracting Image 54 from Image

62 (shown in Fig. 6a) reveals the expected positive signal enhancement in the left motor cortex and negative signal enhancement in the right motor cortex. Note the artifactual signal enhancement in the sagittal sinus region, which is likely to arise from time-of-flight flow effects of CSF or blood (30).

Averaging with Subtraction

The ranges of averaged images are shown in Fig. 5a as solid lines on each side of each dotted line. The average of Images 52 to 57 was subtracted from the average of Images 60 to 65 and displayed in Fig. 6b. Although, the image quality is improved somewhat, the artifactual signal enhancement in the sagittal sinus region is still present.

Cross Correlation

Box-Car "Ideal" Vector. Figure 7a illustrates a first approximation of the activation-induced signal enhancement time course. The box-car waveform can be considered as a 128 dimensional vector. The delay between the induced signal enhancement and neuronal activation is taken into consideration by adjustment of the phase of the box-car waveform. The dot product (i.e., scalar product) of this reference vector with each vector formed by the time-course signal evolution in each pixel is displayed in Fig. 6c. This is a cross-correlation image using

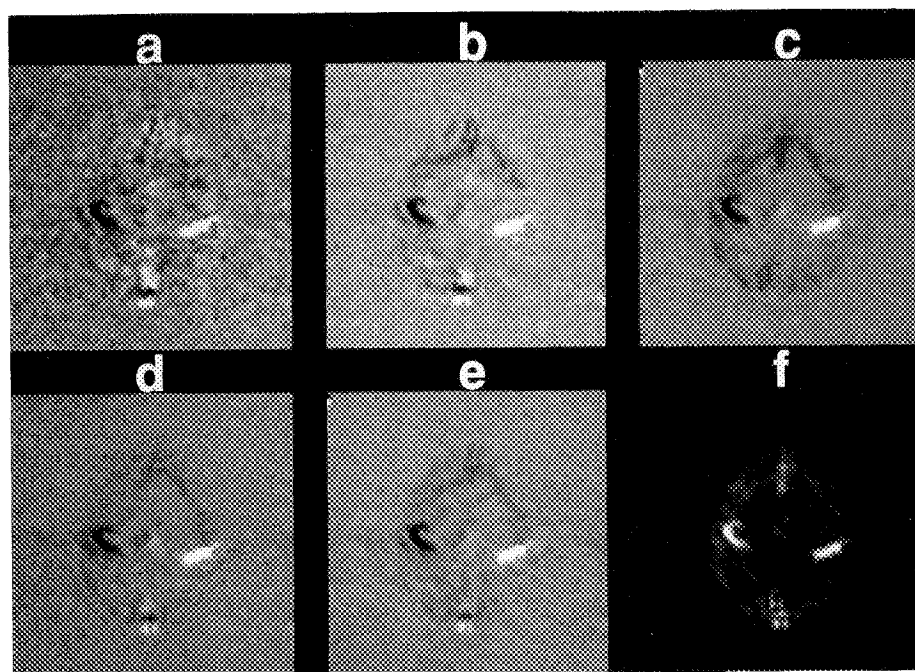


FIG. 6. Functional images from identical time-course series obtained by six different methods. (a) Single image subtraction of Image 54, obtained during peak right motor cortex activation from Image 62 obtained during peak left motor cortex activation (illustrated in Fig. 5 by dotted lines). (b) The average of Images 52 to 57 subtracted from the averaged Images 60 to 65 (illustrated by solid lines in Fig. 5). (c) Cross-correlation image obtained by taking the dot product of each time-course vector with a synthesized box-car vector (displayed in Fig. 7a). (d) Cross-correlation image obtained by taking the dot product of each time-course vector with vector Fig. 5a from the center of Box B. (e) Cross-correlation image obtained by taking the dot product of each time-course vector with the synthesized time-averaged vector of Fig. 7b (see text). (f) Spectral density image. Note that the phase information is lost.

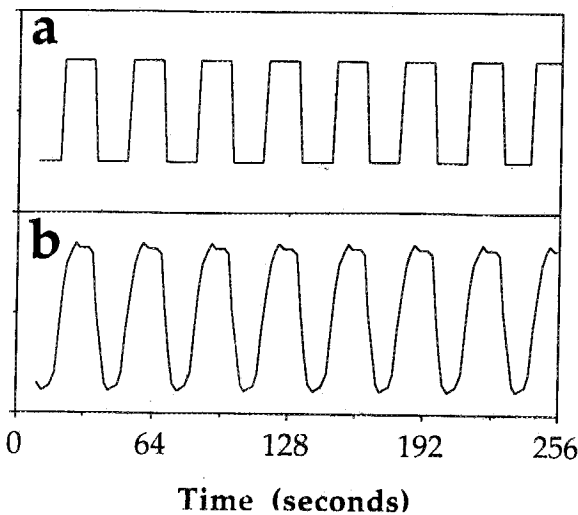


FIG. 7. Synthesized vectors used to create functional images. Both vectors correspond with expected signal enhancement in the left motor cortex (Box B, Fig. 1). (a) Box-car waveform used in creation of the cross-correlation image in Fig. 6c. (b) Time-averaged waveform used in creation of the cross-correlation image in Fig. 6e. (See text.)

a synthesized reference as discussed in the Theory section. The dot product of a box-car waveform and a time-course series is essentially the same as averaging all images during the interleaved "on" periods and subtracting the average of all images during the interleaved "off" periods. Because all 128 images in the time course were used, the contrast-to-noise increases, even though the actual pixel responses do not represent box-car waveforms (13).

Actual Pixel Vector. The temporal response of the MR signal to functional brain activity is an incompletely understood process in which information is transduced from neuronal activity through vascular changes, blood chemistry changes, and field inhomogeneities to changes in the MR signal. Therefore, until an accurate and well parameterized model for functionality induced MR signal changes is established, the use of ideal response vectors as the basis for correlation is necessarily over simplistic. As an alternative, it is useful empirically to select the response of one or more pixels in the actual data set for use as the reference vector. The correlation image using this reference vector is displayed in Fig. 6d. The image quality is improved compared with Fig. 6c (because the reference vector more closely approximates the actual response vectors and the dot products are higher). A problem with using this strategy for creating a reference vector is that any artifactual signal enhancement related to, among other artifacts, gross motion, pulsatility, or flow, may also be present in the reference vector; artifactual signal changes that may occur at various times in the time course will appear correlated to the reference vector. In addition, the noise that is present in the reference vector will correlate with itself, creating an artificially elevated magnitude of correlation in that pixel.

Time-Averaged Response Vector. In this section, we consider use of a reference time-course vector that is formed

by averaging across cycles in time. A time-averaged response vector was produced by averaging each 16-image (32 s) cycle of vector **B** in Fig. 5a, and replicating this time-averaged cycle throughout the time-course vector. The time-averaged-response vector is illustrated in Fig. 7b. The corresponding cross-correlation image using this reference vector is displayed in Fig. 6e. The image quality is improved slightly, although signal enhancement is still present in the artifactual region near the sagittal sinus. The artifactual signal enhancement was not as evident in the image that was created using the box-car reference vector. This may suggest some slight correlation of the signals from the sagittal sinus with a specific aspect of

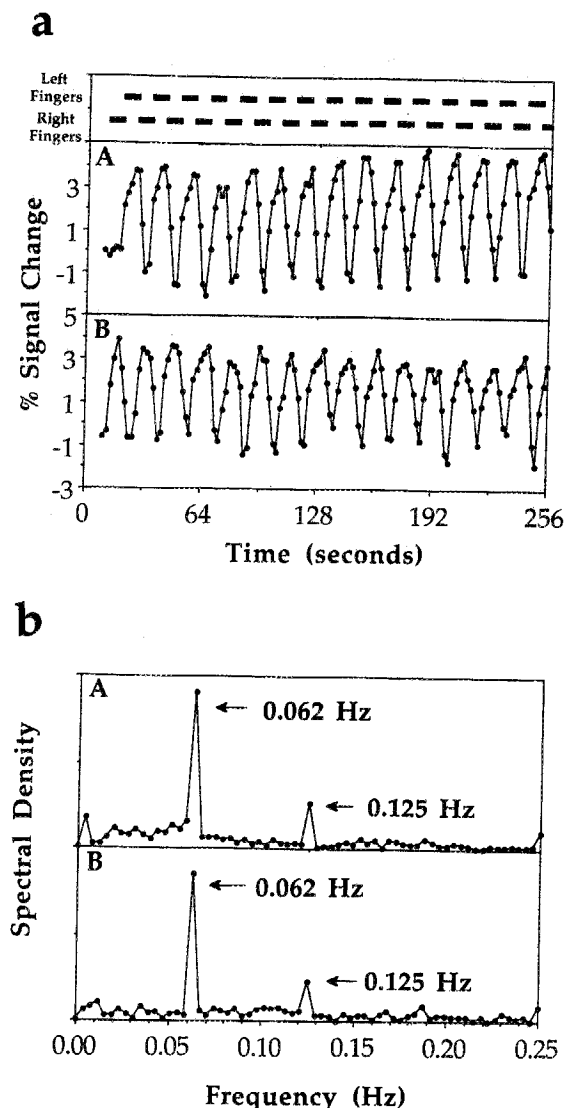


FIG. 8. Plots from the center pixels in Fig. 1. The activation paradigm of interleaved, alternating hand finger movement is shown at the top. The on/off cycle rate is 0.062 Hz. (a) Plots from the center pixels in Boxes A and B show close correspondence with the left and right finger movements, respectively. (b) Plots of the spectral density vs frequency from the center pixels in Boxes A and B reveal sharp peaks at the same frequency, 0.062 Hz. Also evident is response at the second harmonic, 0.125 Hz, indicative of the asymmetric nature of the time course.

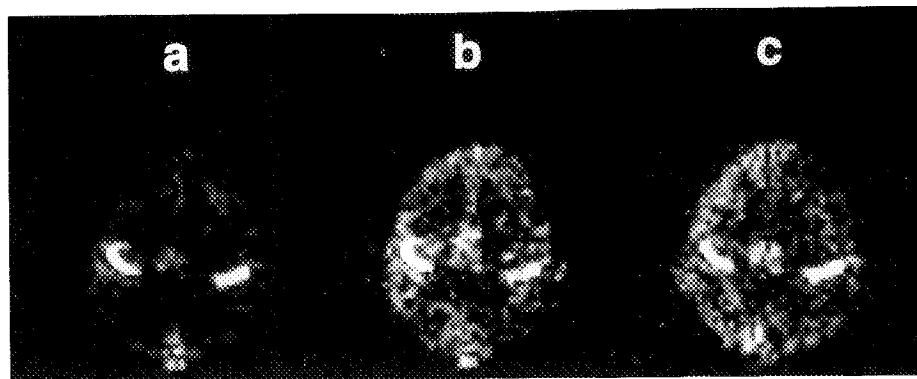


FIG. 9. Functional images obtained by Fourier transform of the time-course data set. (a) Fundamental frequency image at the spectral peak of 0.062 Hz (see Fig. 8b). (b) Second harmonic image at the 0.125 Hz peak. The second harmonic image gives spatial information related to regions that have asymmetric time courses. (c) Fundamental frequency image at the spectral peak of 0.125 Hz (see Fig. 10b), demonstrating that 8-s on/off cycle rates may be used in creation of functional images.

the reference vector. Very high signal-intensity variations with only slight correlation will cause artifacts in a functional image created in this manner. The thresholding method addresses this issue, as will be shown.

Fourier Transform

Figure 5b shows the magnitude of Fourier transforms of the time responses in Fig. 5a. A peak is apparent at 0.031 Hz. The spectral-density image at 0.031 Hz is shown in Fig. 6f. Both motor cortices are switching at identical rates, although, exactly out-of-phase. The activation pattern is the same as that revealed by the cross-correlation techniques. The signal enhancement at the sagittal sinus appears once again and is due to the broad-band effect that occurs with sampling of time-of-flight signal changes that occur throughout the cardiac cycle.

Faster Switching Paradigm. The paradigm was changed so that the subject doubled the switching rate of Fig. 5a. The time courses of the same pixels in the center Boxes A and B are displayed in Fig. 8a along with the Fourier transforms of the corresponding time plots, Fig. 8b. As expected, the peak is shifted to 0.062 Hz. The spectral-density image at this peak (Fig. 9a) reveals the same activation pattern with less artifactual signal enhancement. The cleaner image arises from reduced spurious harmonic content at 0.062 Hz in the original time-course data relative to 0.031 Hz, but the physiological basis for this observation is not well understood.

Higher harmonics are observed in the spectral displays as well. The second harmonic image at the 0.125-Hz peak, indicative of the asymmetric nature (i.e., lack of symmetry about the peak center) of the time response, is shown in Fig. 9b. The activation pattern varies somewhat. The premotor, sensory and supplementary motor regions appear enhanced.

Fastest Switching Paradigm. The switching rate was redoubled to 0.125 Hz. The time courses (Fig. 10a) involve the same pixels used previously. They show an increase in the steady-state baseline because the hemodynamic response is insufficiently rapid to follow the paradigm. Nevertheless, the vascular response is incompletely damped, and from the Fourier transform of the response exhibits a peak at 0.125 Hz (Fig. 10b). The spectral-density image at 0.125 Hz (Fig. 9c) reveals, once again, the same activation pattern as Fig. 9a, but with increased artifactual signal enhancement. This is likely to arise

from a decrease in relative amplitude of the spectral-density peak because of a decrease in the average amplitude change in the time course.

Multiplexed Frequency Switching Paradigm. In using the Fourier transform technique, only the frequency of the activation needs to be known to create a brain function image. An advantage of this analysis technique is that multiple stimuli can be multiplexed into a single time course to reveal activated brain regions in spectral density images that correspond with each activation frequency.

To demonstrate this advantage, a subject was cued to moved the fingers of the right hand at an on/off switching rate of 0.08 Hz, and the fingers of the left hand at 0.05 Hz. The time course consisted of 94 sequentially obtained images. The first image in the time course is shown as a reference in Fig. 11. Figures 12a and 12b are 5×5 pixel matrices of time courses from the regions corresponding to Boxes A and B in Fig. 11. Figure 13a shows the activation timing for each hand and the signal response from the center pixel in each region. It is observed that the time course of Box A (over the right motor cortex) and Box B (over the left motor cortex) follow the activation frequencies of the left and right hands, respectively. The Fourier transform of the data set (Fig. 13b) reveals peaks at 0.08 and 0.05 Hz. Spectral density images at each peak (Figs. 14a and b) reveal enhancement in the right and left motor cortices, respectively, as well as broad-band artifact in the sagittal sinus.

Imaging Formation with Thresholding

Time Domain. A common artifact in time-course data sets occurs near the sagittal sinus or larger vessels. Very intense, seemingly noise-like, fluctuations are seen that are presumably associated with pulsatile flow. Cross-correlation with a reference vector can result in apparent response in these regions even in the absence of induced brain activation. Figure 15 illustrates a *correlation coefficient* image revealing shape correlation during the task activation paradigm of Fig. 5. The waveform of Fig. 7b was used as a reference vector, as was the case for Fig. 6e. Note the difference between a cross-correlation image and a correlation coefficient image: the latter has not been scaled by multiplying by σ_f/σ_r and all pixel values lie between +1 and -1. It is observed that the signal at the sagittal sinus shows minimal correlation. Figure 16a

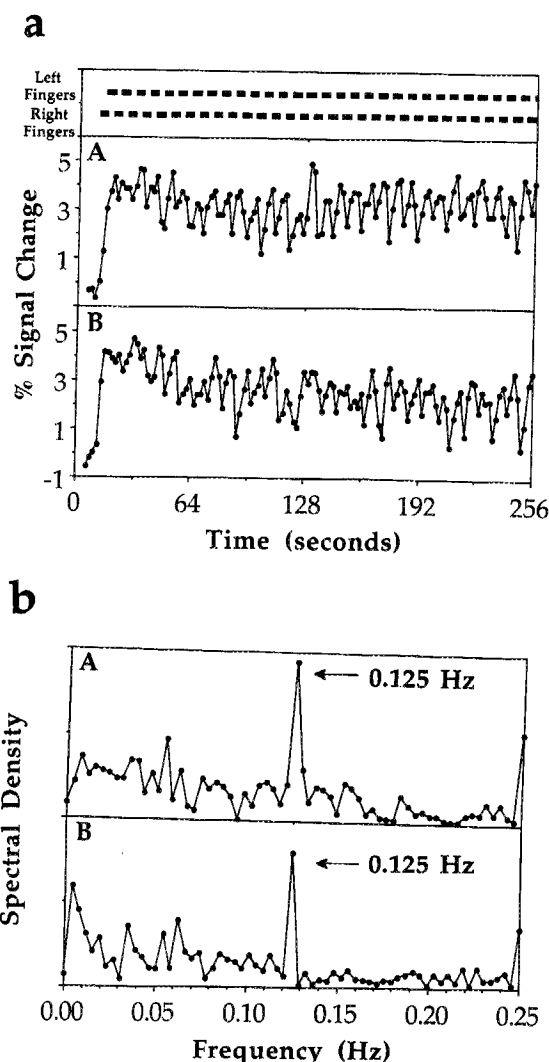


FIG. 10. Plots from the center pixels in Fig. 1. The activation paradigm of interleaved, alternating-hand finger movement is shown at the top. The on/off cycle is 0.125 Hz. (a) Plots from the center pixels in Boxes A and B correspond closely with the left and right finger movements, respectively. Because of the high rate of oscillation, the baseline value is at a higher steady-state level and the oscillation amplitude is reduced; however, the on/off cycle is clear. (b) Plots of the spectral density versus frequency from the center pixels in Boxes A and B reveal sharp peaks at 0.125 Hz. A second harmonic peak, which is indicative of the oscillation cycle asymmetry, is apparent.

shows the same image as in Fig. 6e, but with thresholding applied so that only responses that demonstrate a correlation coefficient >0.25 are used to create the brain function correlation image. Figures 16b and 16c use the same data set, but with thresholds of 0.5 and 0.75, respectively.

The statistical significance for acceptance of signals based on the correlation coefficient is easily determined. The significance P is uniquely related to the selected threshold TH by Eq. [13].

$$P = 1 - \frac{2}{\pi^{1/2}} \int_0^{TH\sqrt{N/2}} e^{-t^2} dt. \quad [13]$$

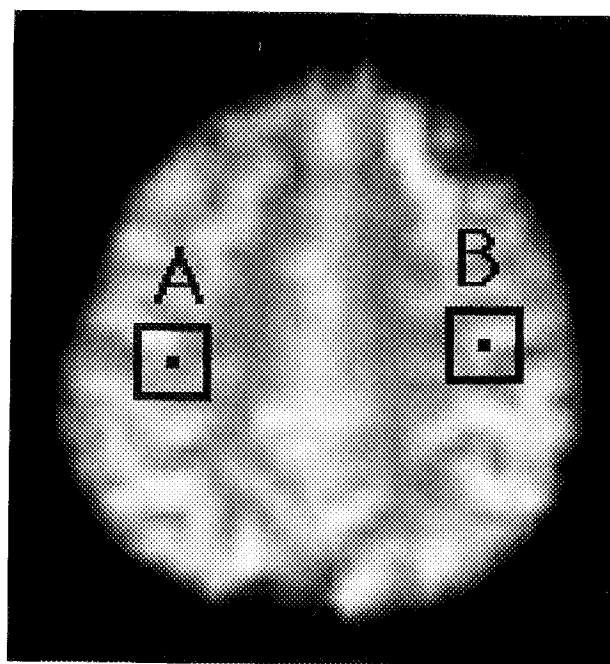


FIG. 11. Axial image showing the motor cortices. Voxel dimensions are $3.75 \times 3.75 \times 10$ mm, $TR/TE = \infty/40$. Boxes A and B are 5×5 pixel regions that presumably cover the right and left motor cortices, respectively. The temporal-spatial plots, shown in Fig. 12, are from the boxed regions. The time-course and spectral plots, shown in Fig. 13, are from the central pixel in each box.

The integral is the complementary error function and P is the probability that the observed correlation coefficient could have occurred by chance. In writing Eq. [13], an assumption is made that the noise has a Gaussian variance about the reference vector, which has not been established. Nevertheless, the equation gives good qualitative insight. In the present work ($N = 128$), a value of $TH = 0.25$ corresponds to $P = 0.005$, and a value of $TH = 0.5$ results in $P = 1.5 \times 10^{-8}$. The use of larger data sets, for example 1024 rather than 128, obviously would reduce the P -values even further. As another qualitative indicator, a value of TH of 0.4 corresponds to a signal-to-noise ratio of about 1 when $N = 100$. For the nonspecialist in statistics, it can be said that if a fairly complicated waveform is readily seen by visual inspection of the data, it is always highly significant.

A color image at a chosen threshold level may be superimposed upon a reference image chosen from the echo-planar time-course series or upon from a high-resolution image that was obtained during the same session such that the images are directly registered. The 0.5 correlation coefficient threshold image is superimposed upon the first image in the time-course series (Fig. 17). The red colors correspond to positive correlation and the blue colors to negative correlation.

Frequency Domain. Formation of cross-correlation images with thresholding can be carried out using not only time-domain data but also frequency-domain data. We have applied this technique to the data acquired using the multiplexed frequency switching paradigm (see Figs.

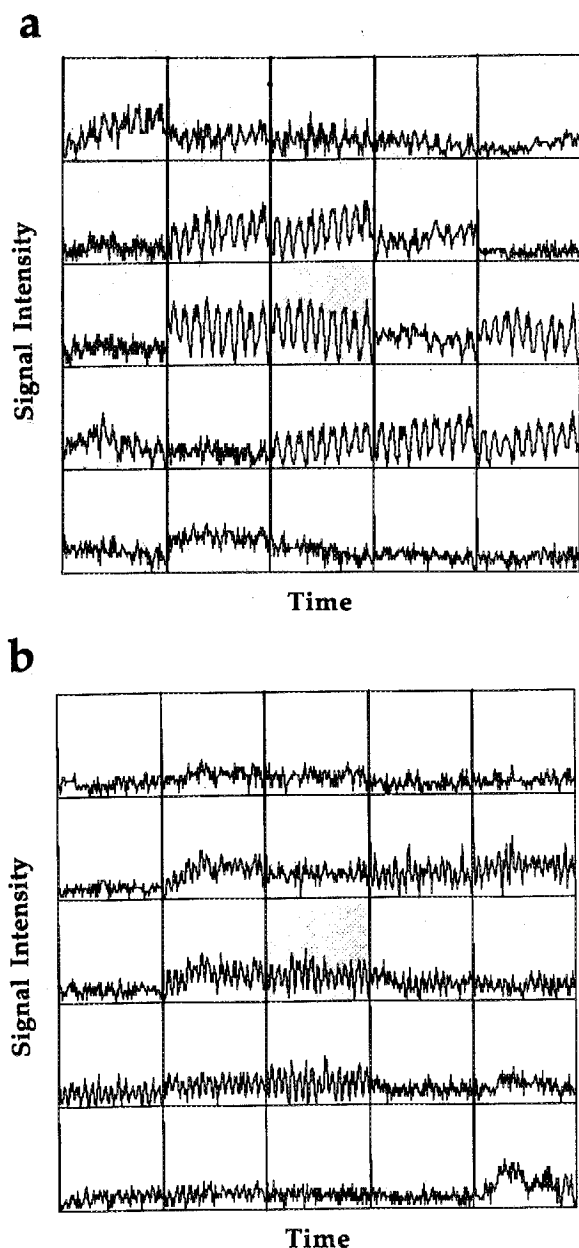


FIG. 12. Temporal-spatial plots from the 5×5 pixel boxes in Fig. 11. The active regions, which are revealed by the signal changes that are temporally correlated with the activation time course, are again sharply outlined and have distinct frequencies that correspond to the different on/off finger movement cycles of each hand. (a) Plot from Box A (right motor cortex). (b) Plot from Box B (left motor cortex).

11–14). Spectral density plots in Boxes A and B of Fig. 13b were used as reference vectors; the threshold was set at $cc = 0.5$; and frequency-domain cross-correlation images were produced, Figs. 18a and 18b, respectively. In this figure, colorized functional images are superimposed on the first anatomical image of the *time-course* data set. Figure 18a shows response only in the left motor cortex and Fig. 18b only in the right. Note that the broadband pulsatile artifacts in the sagittal sinus are removed by the thresholding process.

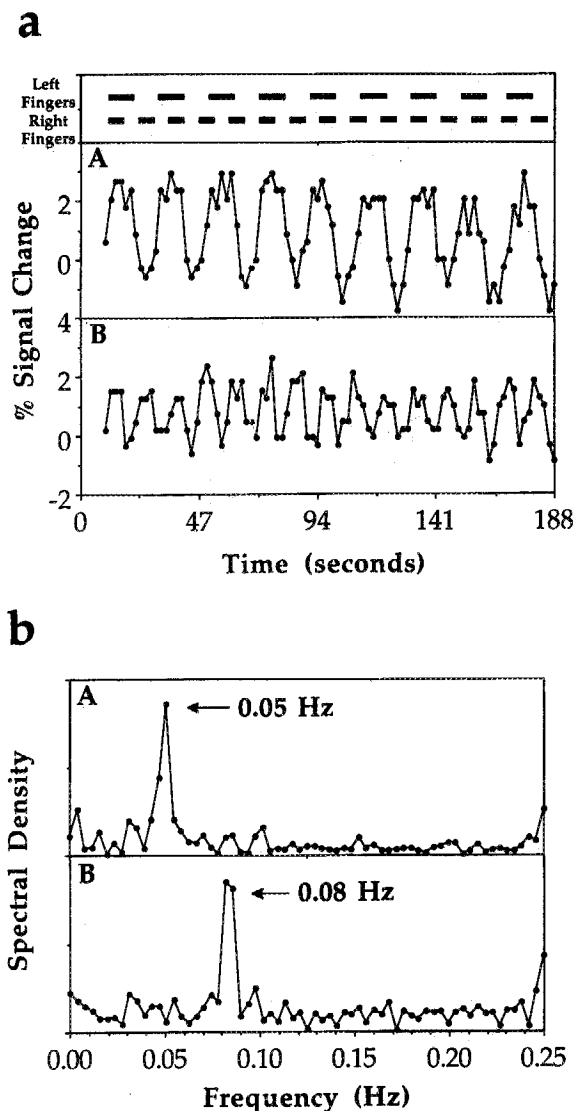


FIG. 13. Plots from the center pixels in Fig. 11. At the top is the activation paradigm that involves on/off frequencies of 0.05 Hz for finger movement of the left hand and of 0.08 Hz for finger movement of the right hand. (a) Plots from the center pixels in Boxes A and B correspond closely with left and right finger movements, respectively. (b) Plots of the spectral density versus frequency from the center pixels in Boxes A and B, which reveal peaks at the activation frequencies that correspond again to the left and right hand activation frequencies, respectively. There were no peaks at frequencies that correspond to sums and differences (i.e., the brain did not function as a "mixer" in this experiment). Note that since the activation frequency for either hand did not occur on a multiple of 0.25/128 spectral points, the actual peak is between two points. This misregistration of the peaks results in slightly noisier functional images.

DISCUSSION AND CONCLUSIONS

Our purpose in this work has been to develop an image processing strategy for FMRI that goes beyond simple subtraction of on- and off-responses to a stimulus. Emphasis has been placed on analysis of data in both the time domain and the frequency domain. In both domains,

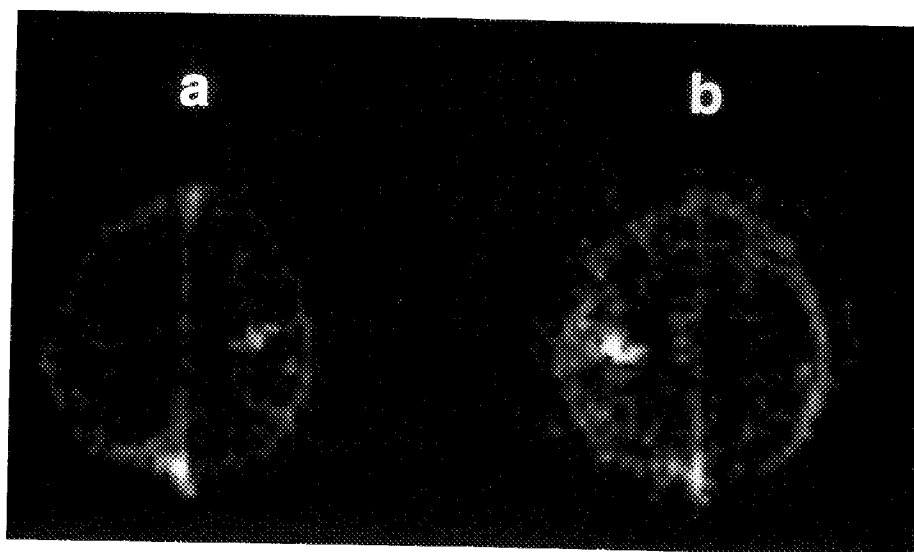


FIG. 14. Functional images obtained from the Fourier transform data set in which finger movement of the left and right hands was at on/off frequencies of 0.05 and 0.08 Hz, respectively. (a) Spectral density image at 0.08 Hz reveals high signal intensity in the left motor cortex. (b) Spectral density image at 0.05 Hz reveals high signal intensity in the right motor cortex.



FIG. 15. Correlation coefficient map of data set from the 0.031-Hz activation paradigm (see text).

thresholding according to the correlation coefficient of the data with respect to a reference waveform serves to reject spurious responses. Formation of the cross-corre-

lation image after thresholding provides a high degree of contrast-to-noise. Several approaches to formation of the reference waveform are described, and this is a central aspect of the methods.

Emphasis has been placed on the mathematics of vector spaces. The geometric approach is not a necessity, and its algebraic equivalent is readily written. However, we are of the opinion that the use of vector spaces is particularly appropriate in the context of FMRI. The mathematics is convenient for Gram-Schmidt orthogonalization of artifactual response vectors with respect to activation response vectors.

Information on the temporal response of the brain can be extracted in several ways: a) Examination of peaks and their relative intensities in the frequency domain display, b) evaluation of the phase information that is presented in the real and imaginary components of the Fourier transformed data, c) study of the cross-correlation coefficient as a function of delay using the time-domain data, and d) variation of rates of activation in the paradigm. Images are readily made that emphasize some aspect of the temporal response. One example, presented here, is an image of the intensity of the second harmonic of the response to a periodic stimulus.

Functional information may be directly registered onto the surface of high-resolution images of the individual's brain. The directly registered information is new to brain

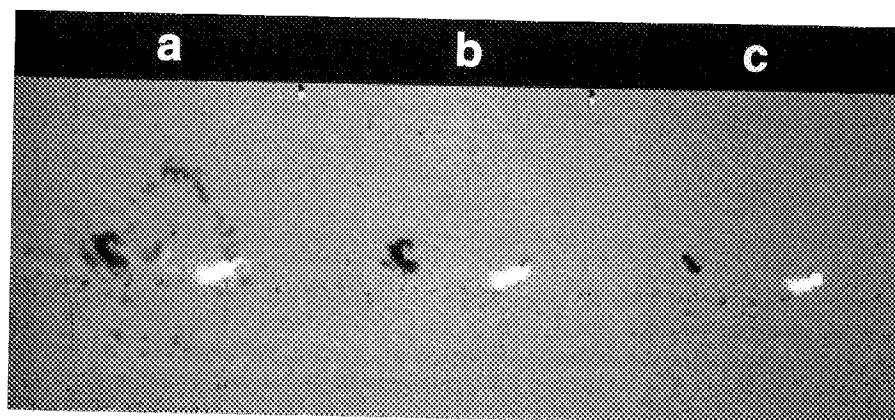


FIG. 16. Thresholded images from the cross-correlation image of Fig. 6e that correspond to selected correlation coefficient (cc) values. In all images, the high signal intensity artifact in the sagittal sinus is removed. Correlation coefficient thresholds: (a) 0.25, (b) 0.50, and (c) 0.75.

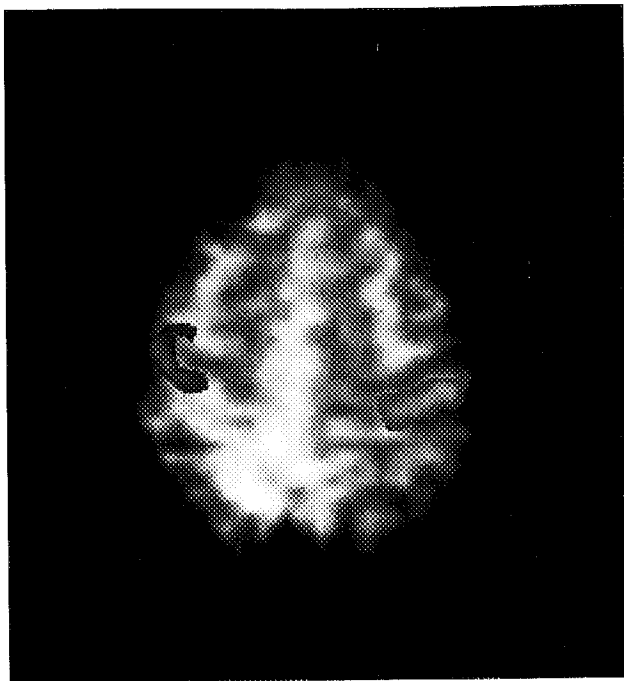


FIG. 17. The image of Fig. 16b (0.5 correlation coefficient threshold) is colorized with red, representing positive correlation, and blue, representing negative correlation. The colorized image is then superimposed on and directly registered with the first anatomical image in the time-course series to create a brain activation image with functional and anatomic information.

imaging modalities. Transformation of the directly-registered functional MRI data to a standardized atlas effectively removes the intrinsically high-resolution gained by the use of functional MRI and may be misleading or even undesirable. The wide intersubject variability of brain structure/function relationships that is generally observed defies standardized mapping techniques. It can now be directly imaged and understood using FMRI.

We have presented an array of activation paradigms and postprocessing tools tailored to the unique nature of time-course FMRI data and artifacts. The use of an entire time-course of rapidly obtained images of the same plane immediately gives signal-to-noise advantages, but with increased artifactual contamination. The control of the activation timing and the application of the postprocessing methods allow effective removal of the artifactual data and reveal potentially useful information about the relative shapes and phases of the time-course responses to neuronal activation. Spatial and temporal brain function information previously unobtainable by other modalities may now be revealed by effective use of the many advantages of these FMRI postprocessing strategies.

ACKNOWLEDGMENTS

The authors thank J. R. Binder, E. A. DeYoe, R. S. Hinks, V. M. Haughton, and S. M. Rao, for helpful discussions; as well as L. D. Estkowski, for technical assistance.

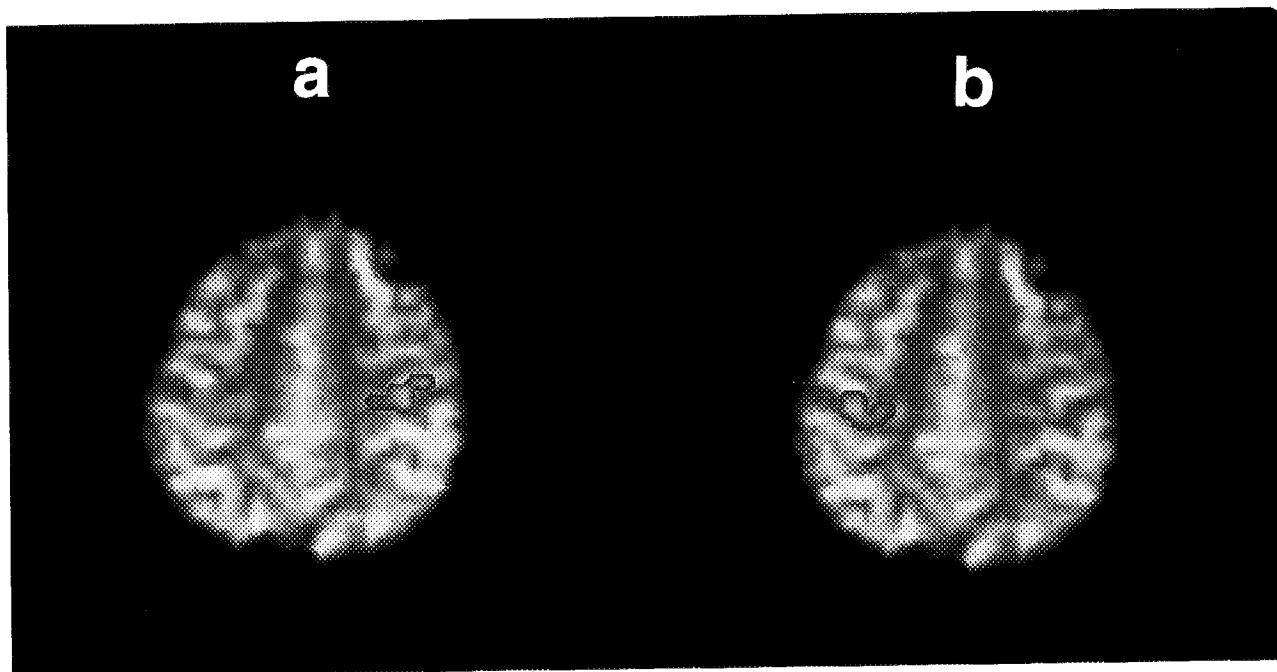


FIG. 18. Images obtained using a 0.5-correlation coefficient threshold against the reference spectra of Fig. 13b. Note that the high signal intensity artifacts in the sagittal sinus are removed. The colorized images are superimposed on and directly registered with the first anatomical image in the series. (a) Brain activation image obtained using the spectral reference vector with the 0.08-Hz peak. Only the left motor cortex region shows enhancement. (b) Brain activation image using the spectral reference vector with the 0.05-Hz peak. Only the right motor-cortex region shows enhancement.

REFERENCES

1. P. T. Fox, M. E. Raichle, *Proc. Natl. Acad. Sci. (USA)* **83**, 1140 (1986).
2. R. D. Frostig, E. E. Lieke, D. Y. Ts'O, A. Grinvald, *Proc. Natl. Acad. Sci. (USA)* **87**, 6082 (1990).
3. R. Turner, D. Le Bihan, C. T. Moonen, D. Despres, J. Frank, *Magn. Reson. Med.* **22**, 159 (1991).
4. S. Ogawa, T. Lee, A. S. Nayak, P. Glynn, *Magn. Reson. Med.* **14**, 68 (1990).
5. S. Ogawa, T. Lee, *Magn. Reson. Med.* **16**, 9 (1990).
6. A. J. De Crespigny, M. F. Wendland, N. Derugin, E. Kozniowska, M. E. Moseley, *Magn. Reson. Med.* **27**, 391 (1992).
7. K. Kwong, B. Hoppel, R. Weisskoff, S. Kiihne, B. Barrere, J. Moore, B. Poncelet, B. Rosen, K. Thulborn, *J. Magn. Reson. Imaging* **2P**, 44 (1992).
8. P. A. Bandettini, E. C. Wong, R. S. Hinks, L. D. Estkowski, J. S. Hyde in "Works in Progress, 11th Annual Science Meeting, Society of Magnetic Resonance in Medicine, 1992," p. 719.
9. P. A. Bandettini, E. C. Wong, L. D. Estkowski, R. S. Hinks, J. S. Hyde, *J. Magn. Reson. Imaging* **3P**, 63 (1993).
10. B. E. Hoppel, R. M. Weisskoff, J. R. Baker, J. B. Moore, K. R. Thulborn, B. R. Rosen, in "Book of Abstracts, 11th Annual Science Meeting, Society of Magnetic Resonance in Medicine, 1992," p. 713.
11. M. K. Stehling, F. Schmitt, R. Ladebeck, *Radiology* **185P**, 198 (1992).
12. K. K. Kwong, J. W. Belliveau, D. A. Chesler, I. E. Goldberg, R. M. Weisskoff, B. P. Poncelet, D. N. Kennedy, B. E. Hoppel, M. S. Cohen, R. Turner, H.-M. Cheng, T. J. Brady, B. R. Rosen, *Proc. Natl. Acad. Sci. (USA)* **89**, 5675 (1992).
13. P. A. Bandettini, E. C. Wong, R. S. Hinks, R. S. Tikofsky, J. S. Hyde, *Magn. Reson. Med.* **25**, 390 (1992).
14. A. M. Blamire, S. Ogawa, K. Ugurbil, D. Rothman, G. McCarthy, J. M. Ellerman, F. Hyder, Z. Rattner, R. S. Shulman, *Proc. Natl. Acad. Sci. (USA)* **89**, 11069 (1992).
15. R. Turner, P. Jezard, H. Wen, K. K. Kwong, D. Le Bihan, T. Zeffiro, R. S. Balaban, *Magn. Reson. Med.* **29**, 277 (1993).
16. J. Sanders, J. George, J. Lewine, A. Caprihan, J. Belliveau, in "Works in Progress, 11th Annual Science Meeting, Society of Magnetic Resonance in Medicine, 1992," p. 1819.
17. J. C. Gore, G. McCarthy, R. T. Constable, A. W. Anderson, R. P. Kennan, Z. Rattner, J. Zhong, in "Works in Progress, 11th Annual Science Meeting, Society of Magnetic Resonance in Medicine, 1992," p. 1826.
18. Y. Cao, V. L. Towle, D. N. Levin, J. M. Balter, *J. Magn. Reson. Imaging* (submitted).
19. J. W. Belliveau, K. K. Kwong, D. N. Kennedy, J. R. Baker, C. E. Stern, R. Benson, P. A. Chesler, R. M. Weisskoff, M. S. Cohen, R. B. H. Tootell, P. T. Fox, T. J. Brady, B. R. Rosen, *Invest. Radiol.* **27**, S59 (1992).
20. J. Frahm, H. Bruhn, K. Merboldt, W. Hänicke, *J. Magn. Reson. Imaging* **2**, 501 (1992).
21. J. Frahm, K. Merboldt, W. Hänicke, *Magn. Reson. Med.* **29**, 139 (1993).
22. S. Ogawa, D. W. Tank, R. Menon, J. M. Ellerman, S. Kim, H. Merkle, K. Ugurbil, *Proc. Natl. Acad. Sci. (USA)* **89**, 5951 (1992).
23. R. S. Menon, S. Ogawa, S. Kim, J. M. Ellermann, H. Merkle, D. Tank, K. Ugurbil, *Invest. Radiol.* **27**, 547 (1992).
24. E. A. DeYoe, J. Neitz, P. A. Bandettini, E. C. Wong, J. S. Hyde, in "Works in Progress, 11th Annual Science Meeting, Society of Magnetic Resonance in Medicine, 1992," p. 1824.
25. A. M. Blamire, S. Ogawa, K. Ugurbil, D. Rothman, G. McCarthy, J. Ellerman, F. Hyder, Z. Rattner, R. G. Shulman, in "Works in Progress, 11th Annual Science Meeting, Society of Magnetic Resonance in Medicine, 1992," p. 1823.
26. E. C. Wong, P. A. Bandettini, J. S. Hyde, in "Book of Abstracts, 11th Annual Science Meeting, Society of Magnetic Resonance in Medicine, 1992," p. 108.
27. E. C. Wong, E. Boskamp, J. S. Hyde, in "Book of Abstracts, 11th Annual Science Meeting, Society of Magnetic Resonance in Medicine, 1992," p. 4015.
28. H. S. Wilf, "Mathematics for the Physical Sciences," Dover, New York, 1962.
29. P. A. Bandettini, E. C. Wong, E. A. DeYoe, J. R. Binder, R. S. Hinks, J. S. Hyde, *J. Magn. Reson. Imaging* **3P**, 89 (1993).
30. K. Butts, S. J. Riederer, *J. Magn. Reson. Imaging* **2**, 285 (1992).